Microstructural design and experimental validation of elastic metamaterial plates with anisotropic mass density

R. Zhu, X. N. Liu, G. L. Huang, H. H. Huang, and C. T. Sun

Phys. Rev. B **86**, 144307 — Published 31 October 2012

DOI: 10.1103/PhysRevB.86.144307

Microstructure design and experimental validation of elastic metamaterial plates with anisotropic mass density

Rui Zhu[1], Guoliang Huang[1*], Hsin-Haou Huang[2], and Chin-Teh Sun[3]

[1]*Deptment of Systems Engineering, University of Arkansas at Little Rock, Little Rock, Arkansas 72204, USA*

[2]*Deptment of Engineering Science and Ocean Engineering, National Taiwan University, Taipei 10617, Taiwan*

[3]*School of Aeronautics and Astronautics, Purdue University, West Lafayette, Indiana 47907, USA*

ABSTRACT

A microstructure design of anisotropic resonant inclusions is investigated for the elastic metamaterial plate with the aid of the numerically-based effective medium model. Experimental validation is then conducted in the anisotropic metamaterial plate through both harmonic and transient wave testing, from which the anisotropic effective dynamic mass density, group and phase velocities are determined as functions of frequency. The strongly anisotropic mass density along two principal orientations is observed experimentally and the prediction from the experimental measurements agrees well with that from the numerical simulation. Finally, based on the numerically obtained effective dynamic properties, a continuum theory is developed to simulate different guided wave modes in the elastic metamaterial plate. Particularly, high-order guided wave coupling and repulsion as well as the preferential energy flow in the anisotropic elastic metamaterial plate are discussed.

* glhuang@ualr.edu; phone 1 501 683-7522; fax 1 501 569-8698

I. INTRODUCTION

Recently, Elastic Metamaterials (EMMs) have gained much attention due to their potential to possess unique effective material properties while maintaining reasonable sample size. Because of the vector characteristics of elastic waves and the possible coupling between longitudinal and transverse modes, richer wave propagation phenomena are expected in the EMMs. Various novel concepts and engineering applications of EMMs have been successfully demonstrated such as mechanical filters, sound and vibration isolators, elastic waveguides and energy harvesters.[1–7] Most of these approaches rely on resonant inclusions and the resulting EMM parameters vary strongly with frequency. In the previous work, the anisotropic effective mass density tensor of an EMM made of lead cylinders coated with elliptical rubbers in an epoxy matrix was numerically determined.[8] However, its practical design and experimental validation have not yet been systematically investigated.

The quest for the anisotropic effective mass density of EMMs has been partly inspired by the success obtained from the Acoustic Metamaterials (AMMs), in which only longitudinal wave mode exists. Cummer and Schurig[9] have numerically presented the possibility of acoustic cloaking by means of AMMs with the anisotropic mass density, however, engineering the AMM was still a challenge at the time. Based on Schoengberg and Sen's work,[10] Cheng *et al.*[11] designed an AMM with the anisotropic mass density by using a concentric alternating homogenous isotropic layered fluid. A feasible method to build and characterize fluid-like cylinders with cylindrically anisotropic mass density has been presented based on the idea that a corrugated structure with radial symmetry can be described by a fluid-fluid multilayered structure.[12] In addition, another new class of AMMs with a dynamical anisotropic effective mass density was numerically designed through two-dimensional anisotropic arrangements of full elastic cylinders embedded in a nonviscous fluid.[13] A similar anisotropic design was suggested in AMMs composed of perforating solid plates in a fluid-like background.[14] Zigoneanu *et al.*[15] presented the experimental realization and characterization of an AMM with strongly anisotropic effective mass density. The metamaterial is composed of arrays of solid inclusions in a background of air, and the anisotropy is controlled by the rotational asymmetry of these inclusions. Most of these

approaches do not rely on resonant inclusions; therefore, the resulting AMM anisotropic parameters vary strongly in a broad frequency range.

Different from AMMs, anisotropy of the effective mass density of EMMs can only be engineered by using anisotropic resonant inclusions instead of anisotropic lattices. Microstructure design of EMMs by embedding rubber coated lead spheres in an epoxy matrix, can be traced back to 2000.[1] The resulting bandgap was later explained by negative effective mass density.[16] Milton and Willis[17] first proposed a two-dimensional (2-D) spring-mass locally resonant model which shows that the effective mass density could become anisotropic. In order to fabricate the EMM with effective anisotropic mass density, Milton[18] suggested a soft-layer-coated elliptic lead core in the solid model, which is modified from the original model proposed by Sheng *et al.*.[19] Gu *et al.*[20] investigated local resonance modes of elliptic cylinders coated with silicon rubber in a rigid matrix to obtain the anisotropic effective mass density. To explain the physical mechanism of the anisotropic mass density, a 2-D lattice model that is composed of anisotropic resonators was studied analytically to obtain a second-order anisotropic effective mass density tensor.[21] However, few EMMs have been fabricated and demonstrated experimentally at structural levels because of the lack of systematic analysis of feasible microstructure designs.

In the paper, we expand upon the previous work[8] and demonstrate experimentally that relatively complex resonant inclusions in a solid plate can create a strongly anisotropic effective mass density. First, the numerically-based effective method is employed to calculate the anisotropic effective mass density tensor of the EMM plate. Thus, a design of the EMM plate with strongly anisotropic mass density is proposed in the continuum manner. The experimental validation is then conducted on the proposed microstructure design of the EMM plate through both harmonic and transient wave testing. Strong anisotropy of the effective mass densities along two principal orientations is obtained and found to be in excellent agreement with the prediction of the numerical simulation. Specifically, the phase and group velocities of the EMM plate are experimentally determined through the transient elastic wave transmission measurements, and its effective dynamic mass density is experimentally determined from the measured phase velocity as a function of frequency.

Finally, to analyze different wave modes in the EMM plate, a continuum model of the EMM plate is developed, and the new wave phenomena such as the wave coupling and repulsion as well as the preferential energy flow are discussed.

II. DESIGN OF EMMs WITH ANISOTROPIC EFFECTIVE MASS DENSITY

Knowing effective dynamic properties of the EMM is a necessary condition for the microstructure design and its wave propagation characteristics. For isotropic EMMs, the three independent effective parameters can be determined: effective bulk modulus, effective shear modulus, and effective mass density.[22, 23] For the EMM with simple microstructures, such as circular-coated spheres or cylinders, the analytically based effective medium theories have been developed.[16, 24] However, in order to design such artificial materials for the desired properties such as anisotropic effective mass density, EMMs must have complex microstructures. For the EMM with general complex microstructures, a numerically-based effective medium model has been recently proposed to determine the effective dynamic properties based on the micromechanics approach.[8, 25] A similar numerical approach was also suggested for EMMs with multi-resonator systems.[26, 27] In this section, the numerically-based effective medium model is adopted for determination of the anisotropic effective mass density of the EMM and its microstructure design.

A. The numerically-based effective medium model

In this subsection, the numerically-based effective medium model is briefly reviewed. Fig. 1 shows a representative volume element (RVE) of the three-dimensional (3-D) EMM, in which the general soft-coated elastic core is embedded in the matrix. The lattice size is denoted as a. The key of this method is to replace the EMM with an equivalent continuous medium under dynamic harmonic loadings. At the macroscopic scale, it is assumed that the composite material will behave as the medium under the applied global deformation. The difficulty of the numerical study is that most standard finite element software does not have the feature to directly deal with the problem with complex variables in the harmonic analysis.

This difficulty can be overcome by solving problems with real and imaginary parts of the constraint conditions separately.[25]

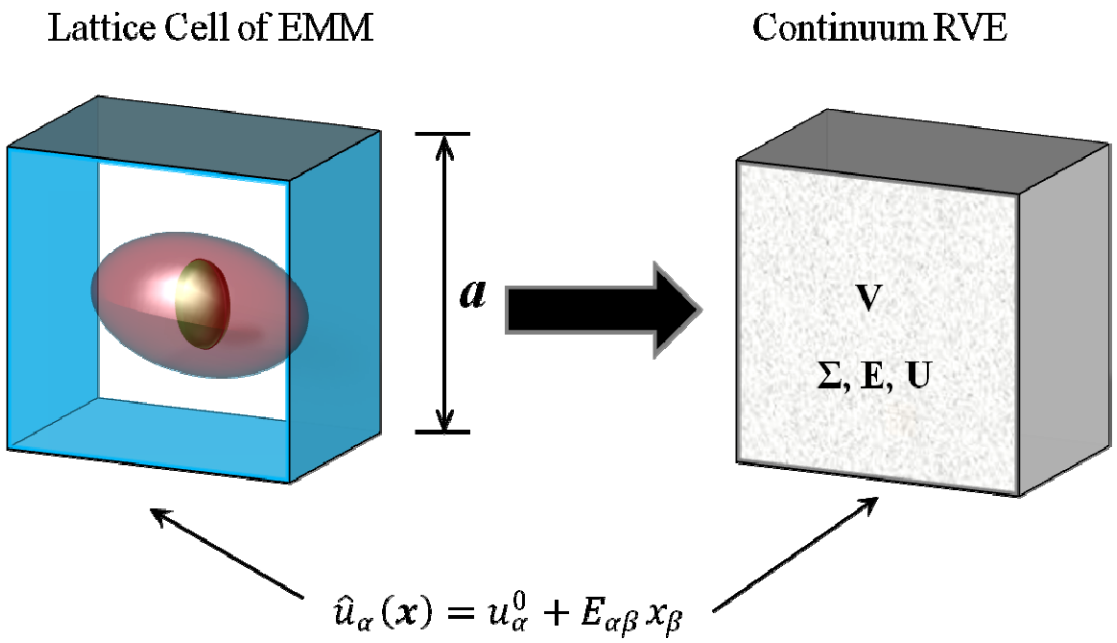

FIG. 1. Representation of EMM lattice cell with arbitrary microstructure by a homogenous solid

The applied local displacement on the boundary of the unit cell can be described as

(1)

where , and is the displacement field compatible with a pre-assumed macro-strain $E_{\alpha\beta}$ plus a rigid translation u^0_α, is the local position vector in the unit cell. The effective medium parameters can then be calculated considering the boundary response of the metamaterial unit cell that "feels" and "responds to" the stimulation exerted by the outside elastic waves. Under the long-wavelength assumption, the effective stress, strain, resultant force and acceleration of the unit cell with the complex microstructure can be obtained by averaging local quantities on the external boundary as:

– —

– –

(2)

where , and are the local stress, displacement and acceleration fields, respectively, with being the boundary unit normal, and denote unit cell's volume and

external boundary. Specifically, the anisotropic effective mass density of the EMM can be determined based on the following relation

$$\begin{bmatrix} F_1 \\ F_2 \\ F_3 \end{bmatrix} = -\omega^2 V \begin{bmatrix} \rho_{11} & \rho_{12} & \rho_{13} \\ \rho_{12} & \rho_{22} & \rho_{23} \\ \rho_{13} & \rho_{23} & \rho_{33} \end{bmatrix} \begin{bmatrix} \widehat{U}_1 \\ \widehat{U}_2 \\ \widehat{U}_3 \end{bmatrix}, \tag{3}$$

where $\widehat{U}_\alpha$is the global displacement field. For example, to calculate the anisotropic effective mass density components: ρ_{11},ρ_{12} and ρ_{13}, the dynamic displacement constraints on the boundary of the RVE are applied as $\widehat{U}_1 = Ae^{iwt}$ and $\widehat{U}_2 = \widehat{U}_3 = 0$. In the principal coordinate system, we have $\rho_{\alpha\beta} = 0$ when $\alpha \neq \beta$. For arbitrary *x*-*y*-*z* coordinate system, it can be numerically proved that the in-plane (*x*-*y* plane) anisotropic effective mass density follows the coordinate transformation law as

$$\begin{bmatrix} \rho_{xx} & \rho_{xy} & \rho_{xz} \\ \rho_{xy} & \rho_{yy} & \rho_{yz} \\ \rho_{xz} & \rho_{yz} & \rho_{zz} \end{bmatrix} = \begin{bmatrix} C & S & 0 \\ -S & C & 0 \\ 0 & 0 & 1 \end{bmatrix} \begin{bmatrix} \rho_{11} & 0 & 0 \\ 0 & \rho_{22} & 0 \\ 0 & 0 & \rho_{33} \end{bmatrix} \begin{bmatrix} C & S & 0 \\ -S & C & 0 \\ 0 & 0 & 1 \end{bmatrix}^{-1}, \tag{4}$$

where $C = cos\delta, S = sin\delta$, δ is the angle between *x*-axis in the arbitrary coordinate system and x_1-axis in the principal coordinate system. Therefore, the effective mass density admits the second-order tensorial property. For the determination of the effective moduli of the EMM, the anisotropic moduli can be similarly obtained based on the constitutive relations. For example, for a 2-D orthogonal EMM, the stiffness tensor can be simplified as only four effective parameters. After obtaining the three effective stresses and three effective strains on the boundary, the effective stiffness parameters can be calculated from the constitutive relations.

B. Design of the EMM plate with anisotropic dynamic mass density

The working mechanism of the EMM with anisotropic effective mass density is fully dependent on the inner microstructure design, which was clearly explained by analyzing the 2-D mass-in-mass lattice model.[21] Based on the mass-in-mass system, the effective mass densities along the two principal directions can be analytically expressed as

$$\rho_{eff,1} = \frac{1}{V}\left(m_1 + \frac{\omega_{0,1}^2}{\omega_{0,1}^2 - \omega^2} m_2\right), \tag{5}$$

$$\rho_{eff,2} = \frac{1}{V}\left(m_1 + \frac{\omega_{0,2}^2}{\omega_{0,2}^2 - \omega^2} m_2\right), \tag{6}$$

where V is the volume of the unit cell, m_1 and m_2 are outer and inner masses, respectively, and $\omega_{0,1} = \sqrt{k_1/m_2}$ and $\omega_{0,2} = \sqrt{k_2/m_2}$ are the locally resonant frequencies of the inner mass along x_1 and x_2 directions, respectively. From Eqs. (5) and (6), it can be found that the anisotropy between $\rho_{eff,1}$ and $\rho_{eff,2}$ is mainly caused by the difference between the locally resonant frequencies $\omega_{0,1}$ and $\omega_{0,2}$, which can be tuned through the design of the internal springs k_1 and k_2 along x_1 and x_2 directions, respectively. Specifically, design of the local stiffness anisotropy in the coating layer is the key to achieve the anisotropic effective mass density of the EMM. In this study, efforts on the microstructure design of the EMM plate with in-plane anisotropic effective mass density will be focused on modification of the well-known three-component sonic crystal, soft-layer-coated heavy core embedded in a matrix. The coating layer with an elliptic shape is suggested to achieve the anisotropic effective mass density of the EMM plate with x_3-axis normal to the plate and in-plane x_1 and x_2 axes are parallel to the elliptical semi-major axis and the semi-minor axis, respectively, as shown in Fig.2 (a). The microstructure geometrical and constituent material parameters are given in Table 1.

TABLE 1. Microstructure geometrical and material parameters.

GEOMETRICAL PARAMETERS		MATERIAL PARAMETERS			
a	11mm		Matrix: aluminum	Coating: epoxy	Core: lead
b_1	4.95mm	Mass density	2700 kg/m^3	1033 kg/m^3	11310 kg/m^3
b_2	3.5mm	Young's modulus	71GPa	0.595GPa	13GPa
Φ	3.175mm	Poisson's ratio	0.32	0.38	0.435
t	3.175mm				

The normalized effective mass densities along x_1 and x_2 directions as functions of the normalized frequency are calculated based on the numerically-based effective medium model, which is shown in Fig. 2 (b). In the figure, ρ_{ave} is the average static mass density for the composite and f_0 is the locally resonant frequency of the microstructure along x_1 direction. It is noticed that $\rho_{eff,1}$ and $\rho_{eff,2}$ have different values in the normalized frequency range from $f/f_0 = 0.4$ to $f/f_0 = 1.8$. However, the anisotropic design is quite limited to the ratio of the semi-major axis to the semi-minor axis of the coating ellipse. To achieve a more strongly anisotropic effective mass density, a more modified microstructure design is needed.

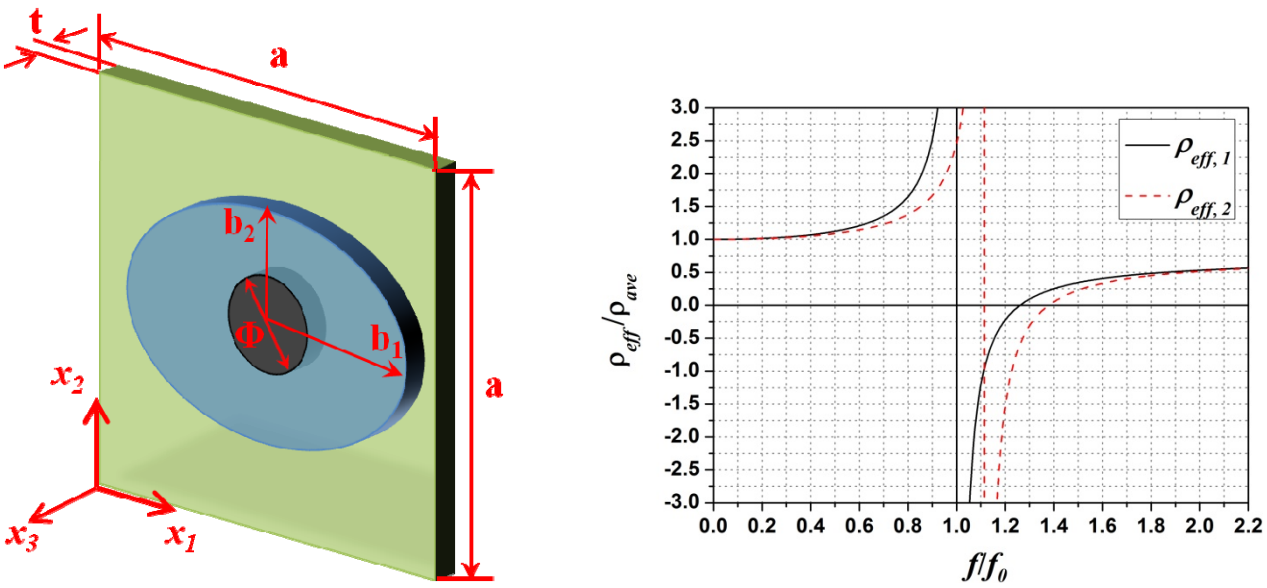

(a) (b)

FIG. 2. (a) Unit cell of the EMM plate with elliptical coating layer. (b) Normalized effective mass densities as functions of the normalized frequency along different principal directions.

Fig. 3 (a) shows a new microstructure design in the elliptical coating layer with four symmetric micro-pores for the greater anisotropy in mass density. The same geometrical and material parameters in Table 1 are used. The diameter of the micro-pore is and the centers of the four symmetric micro-pores are located at with the orientation angles ( ) being respectively. Fig. 3 (b) shows the in-plane normalized effective mass density of the EMM plate with the micro-pores as a function of the normalized frequency. Comparing with the results in the Fig. 2 (b), it can be observed that the lower frequency band of the of and keeps the same, however, the upper band is dramatically increased from to , which shows that stronger anisotropy of the effective mass density can be achieved through the current microstructure design. The same lower frequency band is expected because of the frequency normalization with respect to the static average mass density. It is also interesting to note that the effective mass density becomes isotropic ( ) when the frequency is close to the static case or much larger than the resonant frequencies. The different constant values of the effective mass density in static and high-frequency cases can be explained by Eqs. (5) and (6). It should be mentioned that the anisotropy can be further tuned

through the change of the positions, shapes and sizes of the micro-pores in the coating layer and the inner mass.

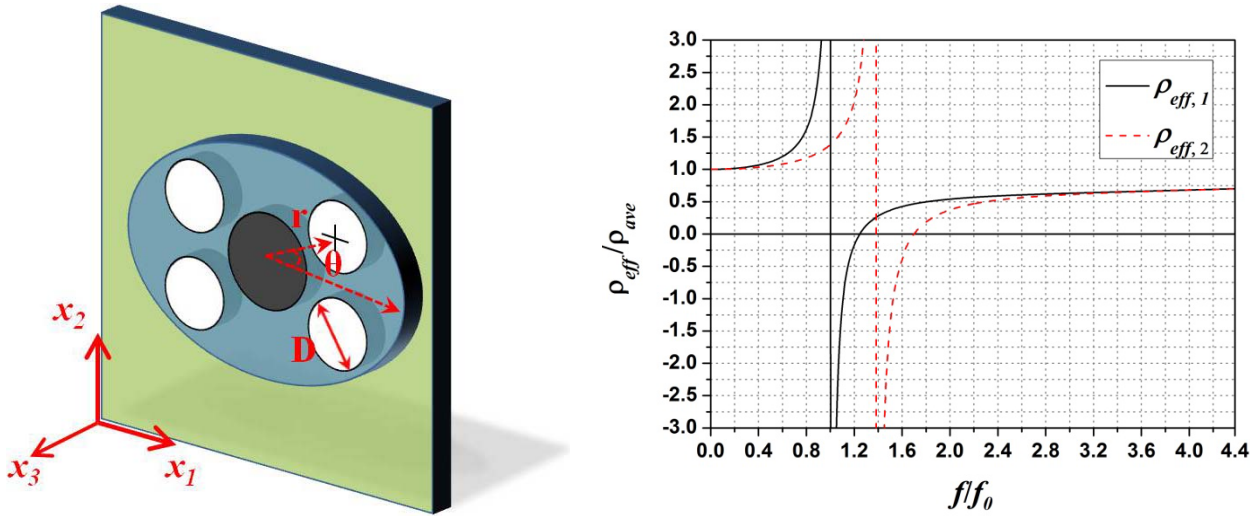

(a) (b)

FIG. 3. (a) Unit cell of the EMM plate with micro-pores in the coating layer. (b) Normalized effective mass densities as functions of the normalized frequency along different principal directions.

III. EXPERIEMENTAL VALIDATION

The experimental testing was conducted on the proposed microstructure design of the EMM plate in Fig. 3 (a). The EMM plates were manufactured with the aid of a computer numerical control (CNC) machine. First, the tests of the harmonic lowest symmetric guided waves along the two in-plane principal directions were performed to demonstrate different bandgaps due to the anisotropic effective mass density of the EMM plate. The group and phase velocity dispersion relations were experimentally determined from measurements of the transmitted transient wave signals with the aid of the wavelet technology, from which the anisotropic effective mass densities of the EMM plate along the principal directions were obtained.

A. The experimental setup

Two anisotropic EMM plates with the proposed microstructure pattern were manufactured for the guided wave propagation tests along the two principal directions. Fig. 4 schematically shows the fabrication procedure of the EMM plate. First, elliptic holes in a rectangular array (10×3) were drilled in the host aluminum (Al) plate (Type 6061) using the CNC machine. Second, pure lead rods (*ESPI Metals*) and liquid epoxy (Crystal Clear® 202, *Smooth-On Inc*) were implanted into the holes. A guiding plate was used to precisely locate the lead rods. After curing, micro-pores in the epoxy coating were formed with the CNC machine. The material properties of the Al plate, cured epoxy and the lead rods are listed in Table 1. The epoxy properties were measured by the simple tension testing of the epoxy samples.

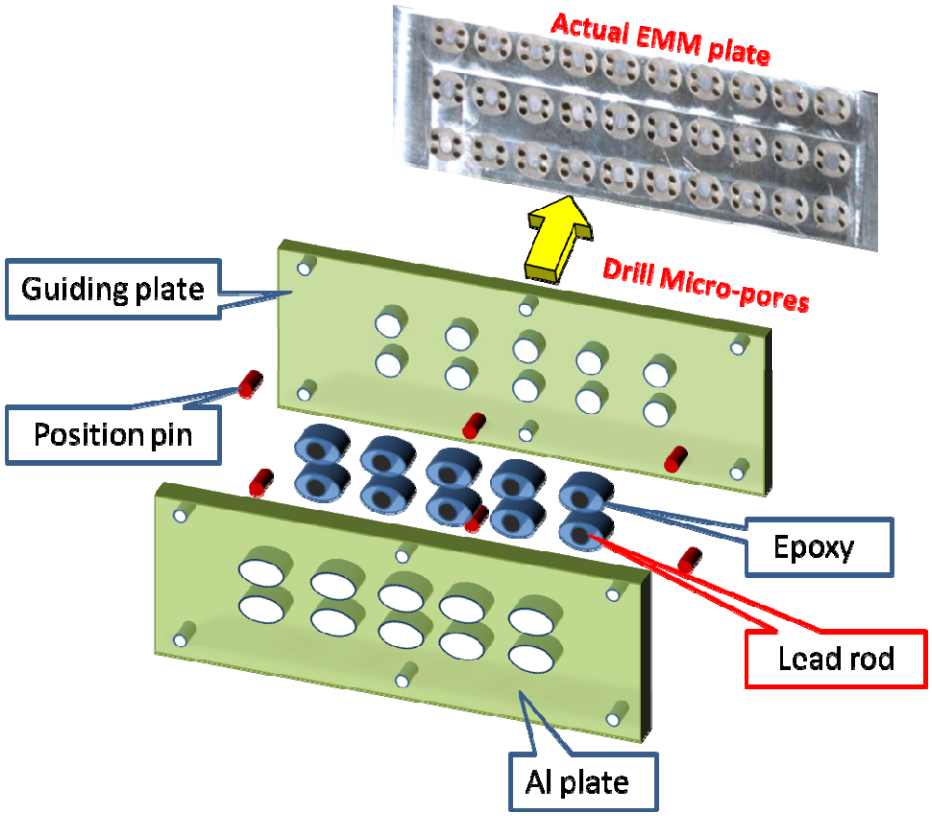

FIG. 4. Schematic diagram of the EMM plate fabrication

To qualitatively investigate the anisotropic dynamic behavior of the EMM plate, the transmission characterizations of the lowest symmetric guided waves propagating in the EMM plates along the two principal directions were first performed experimentally. The experimental set-up, shown in Fig. 5, includes the following components: (1) arbitrary waveform generator (Tektronix AFG 3021) and power amplifier (Krohn-Hite 7602M); (2) two symmetrically surface-bonded rectangular piezoelectric actuators (P-33.00mm-4.00mm-

.76mm-850 WFB, APC International, LTD), as shown in the left zoomed image. The same voltage input is applied on the two actuators to generate the harmonic lowest symmetric guided wave; (3) two circular piezoelectric disks (P-6.36mm-.76mm-850, WFB, APC International, LTD), as shown in the right zoomed image, which are symmetrically surface-bonded on the other side of the EMM plate and functioned as sensors; (4) a digital data acquisition system including a digital oscilloscope (Tektronix DPO4034) and a personal computer for the measurement, storage, and analysis of the received sensor signals. By using the summation of the outputs of both sensors, we can get purely symmetric guided wave signal and efficiently eliminate the unwanted asymmetric wave signal which may come from the slightly position mismatch of the two actuators.

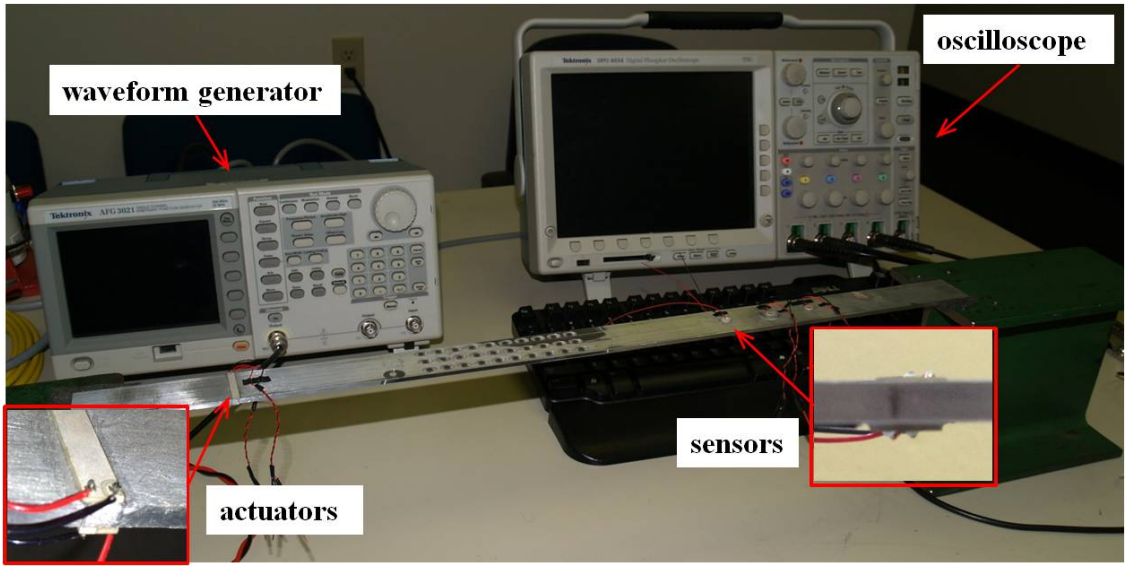

FIG. 5. The experimental set-up for harmonic testing of guided wave propagation in the EMM plate.

B. Wave transmission measurements

Harmonic wave analysis is performed, and the transmitted wave signal of the EMM plate at each harmonic frequency is measured and recorded. By sweeping the frequency of the input harmonic signal, transmitted signals in the interested frequency regime can be secured. Fig. 6 shows the lowest symmetric guided wave transmission of the EMM plates along the two principal directions. For validation purposes, the transmission results of the infinite EMM plates predicted by the numerical simulations are compared with the experimental results.

For wave propagation along x_1 direction, a wave bandgap can be found at the frequency range from 18.2 kHz to 21.8 kHz; however, the wave bandgap is found at the frequency range from 24.8 kHz to 30.4 kHz for wave propagation along x_2 direction. For the current microstructure design, the observed bandgaps can be explained by the negative effective mass density.[16] Therefore, the strong anisotropy of the effective mass density is clearly revealed through the difference of the experimentally measured bandgaps along different wave propagation directions. Very good agreements between the experimental measurement and the numerical prediction also validate the experimental testing.

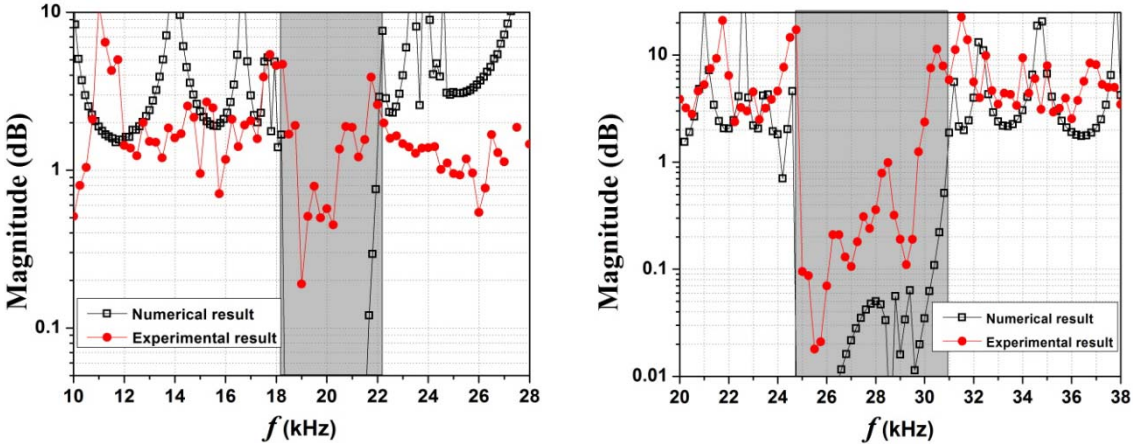

(a) (b)

FIG. 6. Comparisons of numerical and experimental transmission measurements of the lowest symmetric guided wave propagation in the anisotropic EMM plate along (a) x_1 direction and (b) x_2 direction. The shaded regions indicate the corresponding bandgaps predicted by the numerical simulations.

C. Experimental determination of the effective mass density

The effective mass density of the EMM has been analyzed numerically and analytically by numerous methods. However, to the best of our knowledge, experimental determination of the effective mass density of the EMM plate as a function of frequency has not yet been investigated. In order to do that, a transient wave propagation testing in the EMM plate should be conducted to find the group and phase velocities instead of the harmonic wave testing. The main difficulty of the transient wave testing in the solid EMM plate is the wave signal complexity due to the interference by the reflected waves from the two free ends. In

this study, the boundary reflection was eliminated by welding two extended Al plates with the same width and thickness to both ends of the EMM plate. In the experiment, the group and phase velocities cannot be obtained directly from $c_g = \frac{d\omega}{dk}$ and $c_p = \frac{\omega}{k}$, because the time origin of practical collected signals are simultaneously delayed to the time when physical waves excited. Moreover, not all frequency components appear at the same time, a so-called "time lag" exists between different frequency components. Therefore, using two sensors to measure the response waves at the same time can effectively eliminate these side effects. In the study, two symmetrically bonded piezoelectric sensor pairs on the both sides of the EMM plate were used to receive the transient wave signals, as shown in Fig. 7. In the figure, $d = 225mm$ is the distance between two sensor pairs and $d_0 = 110mm$ is the length of the EMM.

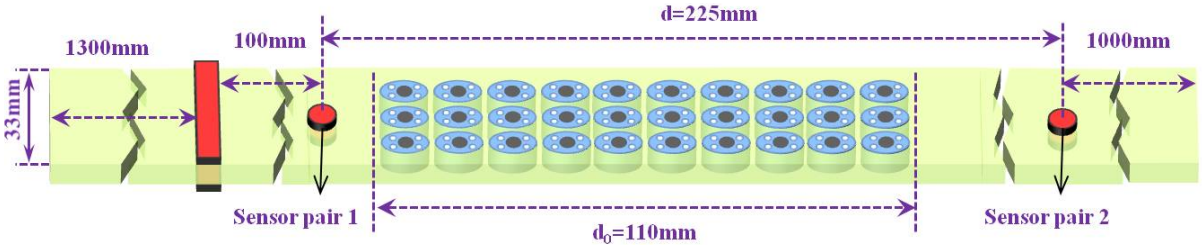

FIG. 7. Schematic diagram of the experimental set-up for the group and phase velocity determinations in the EMM plate

A tune-burst broadband wave signal with the mathematical expression of $V(t) = A_0[1 - \cos(2\pi f_c t)]\sin(2\pi f_c t)$ was chosen, where A_0 is the amplitude and f_c is the central frequency. Different central frequencies in the passing band were selected to cover the frequency regime of interest. Fig. 8 shows the received sensor signals before and after the EMM plate shown in Fig. 7 at the central frequency $f_c = 13.6kHz$, which is within the frequency regime of the passing band. As shown in Fig. 8 (a), the sensor signal collected from the sensor pair 1 is the direct propagating wave signal followed by the strongly reflected wave from the heterogeneous EMM plate. The significant wave dispersion can be found in the transmitted signal collected from the sensor pair 2, as shown in Fig. 8 (b), which makes it very difficult to interpret directly.

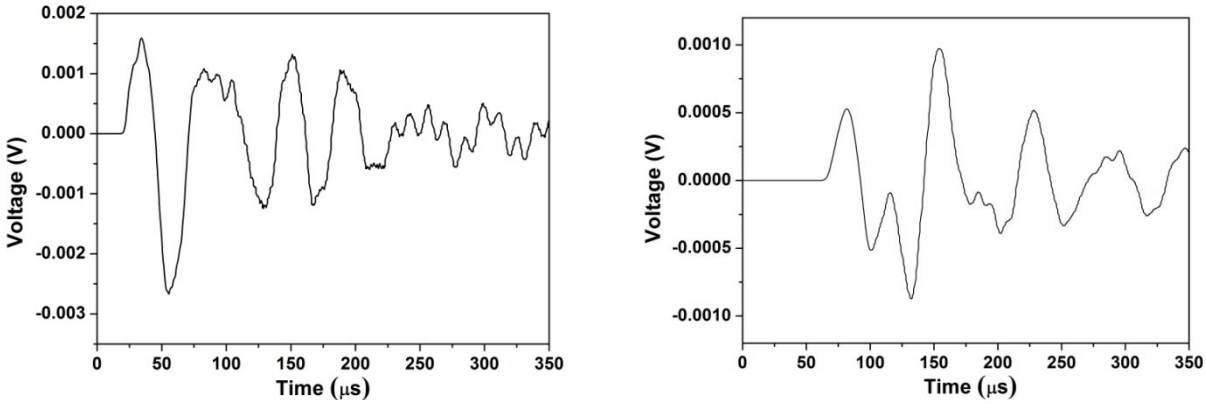

(a) (b)

Fig. 8. The transient wave signals collected from (a) sensor pair 1 and (b) sensor pair 2 at the central frequency $f_c = 13.6kHz$.

1. Determination of group velocity

The continuous wavelet transform (CWT) based on the Gabor wavelets, which has been demonstrated as a useful time-frequency analysis tool of wave signals in structural health monitoring (SHM),[28] is used to obtain the group and phase velocity dispersion curves of the EMM plate. The CWT of a given signal $s(t)$ can be mathematically expressed as follows:

$$WT(\hat{a},\hat{b}) = \frac{1}{\sqrt{\hat{a}}}\int_{-\infty}^{+\infty} s(t)\overline{\psi(\frac{t-\hat{b}}{\hat{a}})}\,dt, \tag{7}$$

where $\psi(t)$ is the mother wavelet function and the overline indicates the complex conjugate, $\hat{a}$ and $\hat{b}$ are known as the scale and translation parameters, respectively. The reciprocal of $\hat{a}$ is associated with the frequency and $\hat{b}$ is related to the time. Gabor function is chosen as the mother wavelet function in the analysis since it can provide better resolutions both in the time and frequency domains than any other wavelets. The Gabor function is expressed as[29]

$$\psi(t) = \frac{1}{\sqrt[4]{\pi}}\sqrt{\frac{\hat{\omega}_0}{\gamma}}\,exp\left[-\frac{(\hat{\omega}_0/\gamma)^2}{2}t^2\right]exp(i\hat{\omega}_0 t), \tag{8}$$

where γ and $\hat{\omega}_0$ are positive constants chosen as $\pi\sqrt{2/ln2} \approx 5.336$ and 2π, respectively. The Gabor function may be considered as a Gaussian window function centered at *t*=0 and its Fourier transform centered at $\omega = \hat{\omega}_0$. Therefore, the CWT using the Gabor wavelet represents the time-frequency component of *s*(*t*) around time $t = \hat{b}$ and frequency $\omega = \hat{\omega}_0/\hat{a}$. For example, Figs. 9 (a) and (b) show the 2D plots of the magnitudes of CWT coefficients of

the measured sensor signals in Figs. 8 (a) and (b), respectively, for a scale with the central frequency $f_c = 13.6kHz$. Physically, the magnitude of CWT reaches its maximum at the wavelet ridge point; the corresponding time $\widehat{b}$ of the ridge point is the group delay which equals the delay of the propagating wave signal envelop, therefore, it can be used in the calculation of the dispersive group velocity at the frequency. The group delays at the two sensor pairs at the frequency are determined by the peak locations of the magnitudes of CWT coefficients of the sensor signals. The difference in the group delays of the waves at two sensor pairs, Δt, is then obtained for the group velocity calculation without side effects.

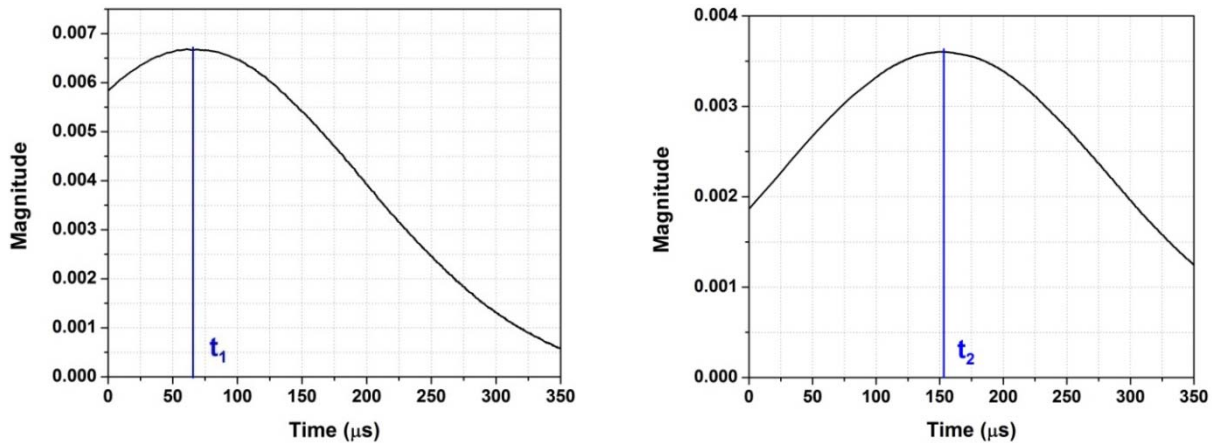

(a) (b)

FIG. 9. The magnitudes of CWT coefficients of the sensor signals collected from (a) sensor pair 1 and (b) pair 2 at $f_c = 13.6KHz$.

In the current sensor deployment, the group velocity as a function of frequency can then be determined with the change of scale as:

$$C_g(f) = d_0/[\Delta t(f) - \frac{d - d_0}{C_g^M}], \tag{9}$$

where $C_g^M = 5400m/s$ is the group velocity in the host Al plate. Fig. 10 shows the measured group velocity of the lowest symmetric guided wave mode in the EMM plate along x_1 direction. For comparison, the group velocity calculated from the theoretical analysis via the relationship $c_g = \frac{d\omega}{dk}$ is also plotted in the figure. The geometrical and material properties used in the calculation are listed in Table 1. Good agreement between the theoretical result and the experimental measurement can be found in both the first and second passing bands.

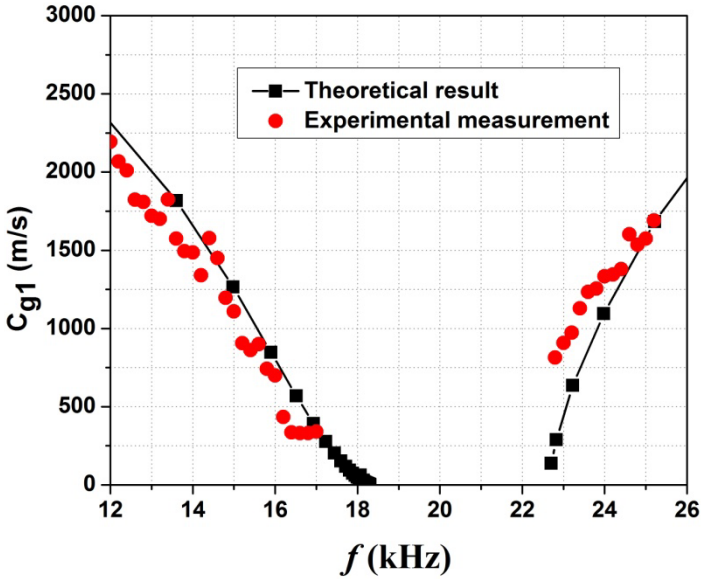

FIG. 10. Experimentally measured group velocity of the lowest symmetric guided wave mode along x_1 direction as a function of frequency.

2. Determination of phase velocity and effective mass density

Determination of the phase velocity of the EMM plate needs the information of the phase angle of the CWT coefficient. At a given scale $\hat{a}$ (frequency), the phase angle of the sensor signal corresponding to certain group delay $\hat{b}$ can be directly determined from the complex CWT coefficient as $\phi(\hat{a}, \hat{b})$, which is in the range of $[-\pi\ ,\ \pi]$. In order to calculate the exact phase difference $\Delta\phi$ between the two sensor signals, the branch number 'm' of the inverse trigonometric function needs to be considered. By using the continuity of the phase spectrum, the proper branch number for each scale can be selected; therefore $\Delta\phi$ can be determined at each frequency. Finally the phase velocity of the EMM plate as a function of frequency can be obtained using the following relation:

$$C_p(f) = \frac{d_0}{(\Delta t(f) + \frac{\Delta\phi(f)}{2\pi f} - \frac{d - d_0}{C_p^M})} \tag{10}$$

where Δt is the difference of the arrival time, and C_p^M is the phase velocity in the host plate. With the change of scale, the dispersive phase velocity versus the frequency can be finally obtained. Fig. 11 shows the phase velocity of the EMM plate from the measured sensor signals. For comparison, the phase velocity predicted from the theoretical dispersion relation

of the EMM plate is also added. In general, the measured phase velocity matches well with that from the theoretical prediction in the frequency range of two lowest passing bands. Good agreement can be found in the frequency range of weak dispersion, however, small discrepancy can be observed in the range of strong dispersion such as the frequency range close to the bandgap.

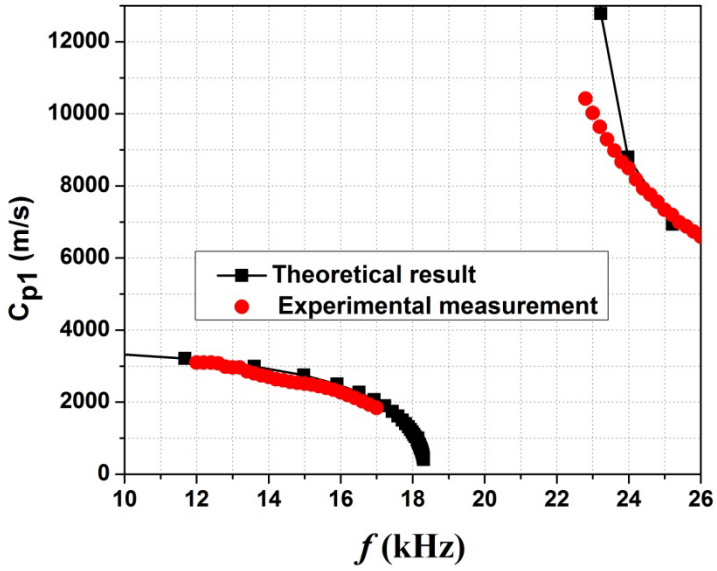

FIG. 11. Experimentally measured phase velocity of the lowest symmetric guided wave mode along x_1 direction as a function of frequency.

Finally, the anisotropic effective mass density of the EMM plate can be determined by the experimentally measured phase velocity and the effective stiffness predicted by the numerically-based effective medium model. For example, for the lowest symmetric guided wave propagating along the principal x_1 direction, the effective mass density of the EMM plate along the wave propagating direction can be determined by $\rho_1(f) = C_{11}^{eff}/[C_{p1}(f)]^2$. Fig. 12 shows the obtained effective mass densities as functions of the frequency for wave propagation along two principal directions based on the experimental data. For comparison, the corresponding effective mass densities from the numerical solutions are also plotted. Excellent agreement can be observed even for the frequency range with strong wave dispersion. It should be noticed that the distribution of the locally resonant elements in the EMM plate will not affect its effective dynamic mass density, which is different from the AMM, because the anisotropic effective mass density of the EMM plate is mainly caused by the anisotropic resonant motion of the locally resonant element.

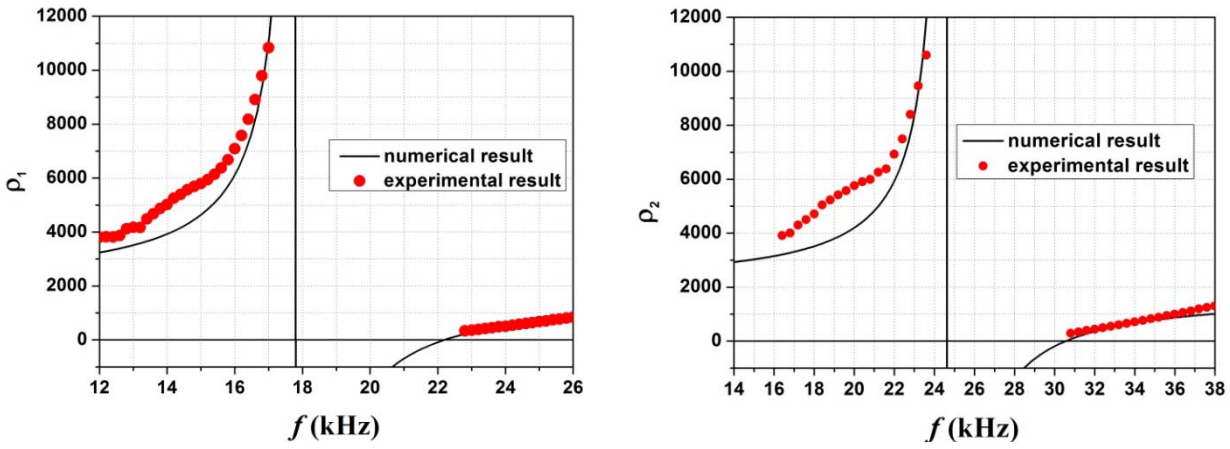

(a) (b)

FIG. 12. Effective dynamic mass densities of the anisotropic EMM plate along the two principal directions: (a) x_1 direction; (b) x_2 direction.

IV. CONTINUUM MODELING OF THE EMM PLATE

The dynamic behavior presented in the previous sections can be further modeled by using analytical approaches which provide more insight into the behavior of the system when undergoing internal resonance. The investigation developed here aims at developing an effective continuum model for different guided wave modes in the EMM plate, which are difficult to be measured experimentally. The analytical results are compared with the experimental measurements and the numerical simulations in different EMM plates. Some interesting dynamic phenomena will be discussed such as high-order guided wave coupling and repulsion in the anisotropic EMM plate. The developed effective continuum model can be applied to problems of time-dependent vibration and transient wave propagation in the EMM plate, which is important for its potential engineering applications.

In general, based on the numerically determined effective stiffness, the 3-D stress-strain relation of the EMM plate in the principal coordinate system can be expressed as:

$$\begin{Bmatrix}\sigma_{11}\\ \sigma_{22}\\ \sigma_{33}\\ \tau_{23}\\ \tau_{13}\\ \tau_{12}\end{Bmatrix}=\begin{bmatrix}C_{11} & C_{12} & C_{13} & 0 & 0 & 0\\ C_{12} & C_{22} & C_{23} & 0 & 0 & 0\\ C_{13} & C_{23} & C_{33} & 0 & 0 & 0\\ 0 & 0 & 0 & C_{44} & 0 & 0\\ 0 & 0 & 0 & 0 & C_{55} & 0\\ 0 & 0 & 0 & 0 & 0 & C_{66}\end{bmatrix}\begin{Bmatrix}\varepsilon_{11}\\ \varepsilon_{22}\\ \varepsilon_{33}\\ \gamma_{23}\\ \gamma_{13}\\ \gamma_{12}\end{Bmatrix}. \tag{11}$$

In an arbitrary *x*–*y*-*z* coordinate system (in-plane: *x*-*y* plane, out-of-plane: *z* axis), the constitutive equations can be derived using coordinate transformation and written as

$$\begin{Bmatrix}\sigma_x\\ \sigma_y\\ \sigma_z\\ \tau_{yz}\\ \tau_{xz}\\ \tau_{xy}\end{Bmatrix}=\left[\bar{C}_{ij}\right]\begin{Bmatrix}\varepsilon_x\\ \varepsilon_y\\ \varepsilon_z\\ \gamma_{yz}\\ \gamma_{xz}\\ \gamma_{xy}\end{Bmatrix}, \tag{12}$$

where $\bar{C}_{ij}$, $i,j = 1$ to 6, are the transformed elastic constants. The equations of motion for the continuum plate with anisotropic mass density tensor can be written as

$$\begin{aligned}\sigma_{x,x}+\tau_{xy,y}+\tau_{xz,z}&=\rho_{xx}\ddot{u}+\rho_{xy}\ddot{v}+\rho_{xz}\ddot{w},\\ \tau_{xy,x}+\sigma_{y,y}+\tau_{yz,z}&=\rho_{xy}\ddot{u}+\rho_{yy}\ddot{v}+\rho_{yz}\ddot{w},\\ \tau_{xz,x}+\tau_{yz,y}+\sigma_{z,z}&=\rho_{xz}\ddot{u}+\rho_{yz}\ddot{v}+\rho_{zz}\ddot{w}.\end{aligned} \tag{13}$$

For the proposed metamaterial plate, the traction-free boundary conditions on the top and bottom surfaces are

$$\sigma_z=\tau_{xz}=\tau_{yz}=0, \qquad z=\pm h/2. \tag{14}$$

For a guided wave along *x* direction, the displacements can be assumed as the form

$$u=Ae^{ikpz}e^{i[k_x x-\omega t]}, \qquad v=Be^{ikpz}e^{i[k_x x-\omega t]}, \qquad w=Ce^{ikpz}e^{i[k_x x-\omega t]}, \tag{15}$$

where $k_x=\omega/c_p$ is the wave number, ω is the angular frequency, c_p is the phase velocity and p is a unknown variable to be determined. Substituting Eqs. (12) and (15) into Eq. (13), we have the following matrix form

$$\begin{bmatrix}\Gamma_{11} & \Gamma_{12} & \Gamma_{13}\\ \Gamma_{12} & \Gamma_{22} & \Gamma_{23}\\ \Gamma_{13} & \Gamma_{23} & \Gamma_{33}\end{bmatrix}\begin{Bmatrix}A\\ B\\ C\end{Bmatrix}=0, \tag{16}$$

where

$$\begin{aligned}\Gamma_{11}&=\bar{C}_{11}+\bar{C}_{55}p^2-\rho_{xx}c_p^2,\\ \Gamma_{12}&=\bar{C}_{16}+\bar{C}_{45}p^2-\rho_{xy}c_p^2,\\ \Gamma_{13}&=(\bar{C}_{13}+\bar{C}_{55})p-\rho_{xz}c_p^2,\\ \Gamma_{22}&=\bar{C}_{66}+\bar{C}_{44}p^2-\rho_{yy}c_p^2,\\ \Gamma_{23}&=(\bar{C}_{36}+\bar{C}_{45})p-\rho_{yz}c_p^2,\\ \Gamma_{33}&=\bar{C}_{55}+\bar{C}_{33}p^2-\rho_{zz}c_p^2.\end{aligned}$$

In order to obtain a nontrivial solution of Eq. (16), the following sixth-order polynomial needs to be satisfied:

$$p^6 + \alpha_1 p^4 + \alpha_2 p^2 + \alpha_3 = 0, \tag{17}$$

where α_l $(l = 1, 2, 3)$ are functions of the stiffness matrix $\bar{C}_{ij}$ $(i, j = 1 \text{ to } 6)$, the effective mass density ρ_{rs} $(r, s = x, y, z)$ and the phase velocity c_p.

By solving Eq. (17), the displacements can take the following summation forms as

$$u = \left(\sum_{j=1}^{6} A_j e^{ikp_j z}\right) e^{i[k_x x - \omega t]}, \qquad v = \left(\sum_{j=1}^{6} B_j e^{ikp_j z}\right) e^{i[k_x x - \omega t]},$$
$$w = \left(\sum_{j=1}^{6} C_j e^{ikp_j z}\right) e^{i[k_x x - \omega t]}, \tag{18}$$

where for each p_j $(j = 1 \text{ to } 6)$

$$B = RA, \qquad R = \frac{\Gamma_{11}\Gamma_{23} - \Gamma_{12}\Gamma_{13}}{\Gamma_{13}\Gamma_{22} - \Gamma_{12}\Gamma_{23}},$$
$$C = SA, \qquad S = \frac{\Gamma_{11}\Gamma_{23} - \Gamma_{12}\Gamma_{13}}{\Gamma_{12}\Gamma_{33} - \Gamma_{23}\Gamma_{13}}.$$

Substituting Eq. (18) into Eq. (14), we have

$$\sum_{j=1}^{6} (H_{1j}, H_{2j}, H_{3j}) A_j e^{\pm ikp_j h/2} = 0 \tag{19}$$

where

$$H_{1j} = \bar{C}_{13} + \bar{C}_{33} p_j S_j + \bar{C}_{36} R_j$$
$$H_{2j} = \bar{C}_{44} p_j R_j + \bar{C}_{45}(p_j + S_j)$$
$$H_{3j} = \bar{C}_{45} p_j R_j + \bar{C}_{55}(p_j + S_j)$$

The existence of a nontrivial solution of Eq. (19) leads to two independent dispersion relations

$$H_{11}(H_{23}H_{35} - H_{25}H_{33}) \cot\left(\frac{kp_1 h}{2}\right) + H_{13}(H_{25}H_{31} - H_{21}H_{35}) \cot\left(\frac{kp_3 h}{2}\right)$$
$$+ H_{15}(H_{21}H_{33} - H_{23}H_{31}) \cot\left(\frac{kp_5 h}{2}\right) = 0 \tag{20}$$

$$H_{11}(H_{23}H_{35} - H_{25}H_{33}) \tan\left(\frac{kp_1 h}{2}\right) + H_{13}(H_{25}H_{31} - H_{21}H_{35}) \tan\left(\frac{kp_3 h}{2}\right)$$
$$+ H_{15}(H_{21}H_{33} - H_{23}H_{31}) \tan\left(\frac{kp_5 h}{2}\right) = 0 \tag{21}$$

which correspond to symmetric and antisymmetric wave modes, respectively.

To validate the continuum model, dispersion relations obtained from the current model will be compared with those from the FE simulation based on the detailed microstructures. We consider the EMM plate with the unit cell shown in Fig. 3 (a). In the first example, the microstructure geometrical and material parameters are given in Table 1 and wave propagation along principal direction is considered. The effective stiffness matrix of the EMM plate can be obtained by using the numerically-based effective medium model, which is listed in Table 2.

TABLE 2. Effective stiffness matrix of the EMM plate (unit: GPa)

36.64	5.57	13.53	18.83	7.84	48.38	12.41	6.69	2.272

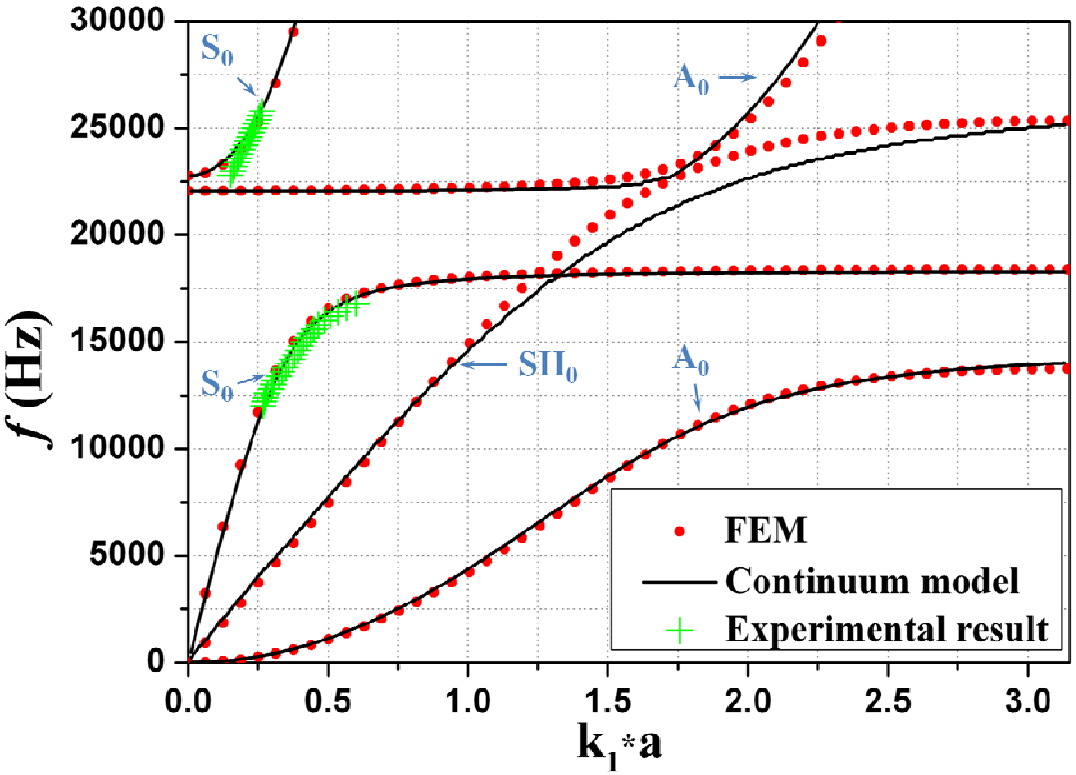

FIG. 13. Comparison of the dispersion curves obtained by the continuum model, FE simulation and experimental measurement for the guided wave along the principal direction

Fig. 13 shows the dispersion relation in the first Brillouin zone of guided wave propagation along principal direction in the EMM plate obtained from the continuum model, which includes the lowest symmetric (S_0) and antisymmetric (A_0) guided wave modes and shear

horizontal (SH_0) wave mode. For comparison, the dispersion relations predicted by the FE simulation based on the exact microstructure and the experimental measurement are also plotted in the figure. The bandgap for the lowest symmetric guided wave can be found in the frequency range of [17.7kHz, 22.8kHz], which has very good agreement with that from the experimental results. For the lowest antisymmetric guided wave and the shear horizontal wave, excellent agreement between the predictions of the current model and the exact FE simulation is found at low frequency range but small discrepancy at higher frequency regime.

To understand wave behavior of different guided wave modes in the EMM plate, a guided wave propagating along a 45 degree with respect to the principal x_1 direction is studied. In the example, to demonstrate engineering application of metamaterial plate in the low-frequency bandgap range, the rubber-coated lead cores are embedded in the epoxy matrix, with material properties for lead ($\rho_C = 11310\,kg/m^3, E_C = 13GPa, \nu_C = 0.435$), epoxy ($\rho_M = 1110\,kg/m^3, E_M = 4.4GPa, \nu_M = 0.38$) and rubber ($\rho_{CT} = 1300\,kg/m^3, E_{CT} = 10MPa, \nu_{CT} = 0.499$), and the geometrical parameters of the microstructure are the same as those in Table 1. The anisotropic effective mass density tensor and the effective stiffness matrix are similarly obtained by using the numerically-based effective medium model. Fig. 14 (a) shows the comparison of dispersion relations in the first Brillouin zone from the continuum model and the numerical simulation based on the exact microstructure, where ω_0 is the locally resonant angular frequency of the microstructure along x_1 direction and $k^* = (k_1 a + k_2 a)/2$. Excellent agreement can be observed in the two lowest order modes because the coupling of the difference wave modes does not occur.

More complicated wave repulsions can be observed in the high-order wave mode diagram from the dispersion prediction by the exact numerical simulation; however, they cannot be predicted by the current continuum model. To give more intuitive understanding of the wave repulsion, the displacement fields of eigenmodes at several gap-edge frequencies marked in Fig. 14 (a) (the points 1-10) are plotted in Fig. 14 (b) to show the physical mechanism of the wave repulsion. From Fig. 14 (b), it can be found that the dispersion curve containing points 1, 7 and 9, which can also be predicted by the continuum model, describes the out-of-plane dominant motion. The wave repulsion, which is reflected at points 2 and 6, is caused by the

local rotation resonance (*x*-*z* plane) in the core. Therefore, it is understandable that the continuum model cannot capture this motion. As a result of the repulsion, the mode coupling can also be observed. For example, the displacement field in the lowest antisymmetric guided wave mode is dominated by the out-of-plane plate motion, as shown in Fig. 14 (b1), below the local rotation resonant frequency while is dominated by a coupling motion between the plate motion and local resonance motion above the local rotation resonant frequency, as shown in Fig. 14 (b7) and (b9). An additional flat band is found from the exact numerical simulation, which cannot be reflected from the continuum model at the frequency $\omega/\omega_0 = 1.6$. From the displacement fields at points 3 and 8, it can be found that the narrow passing band is caused by the local rotation resonance (*x*-*y* plane) in the coating medium, which cannot be captured by the current continuum model. The difference between the current model and the exact numerical simulation is found for the high-order wave modes, the corresponding displacement fields are plotted in Fig. 14 (b) at points 4, 5 and 10. From the displacement fields at points 4, 5 and 10, it can be seen that the high-order wave modes are also the coupling modes of the plate motions and local rotation resonant motion. Therefore, the difference between the two models is due to the coupling behavior, which cannot be captured by the continuum model.

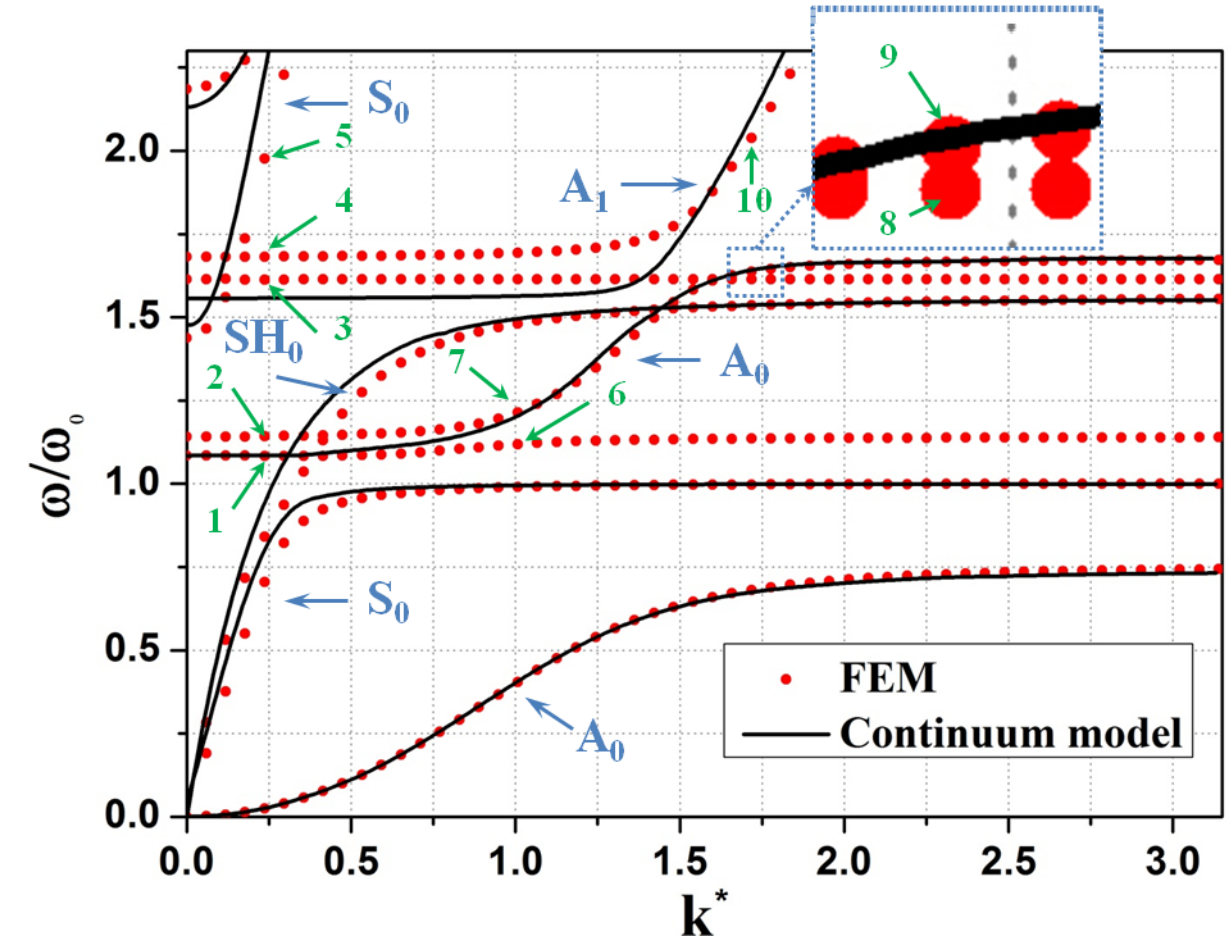

(a)

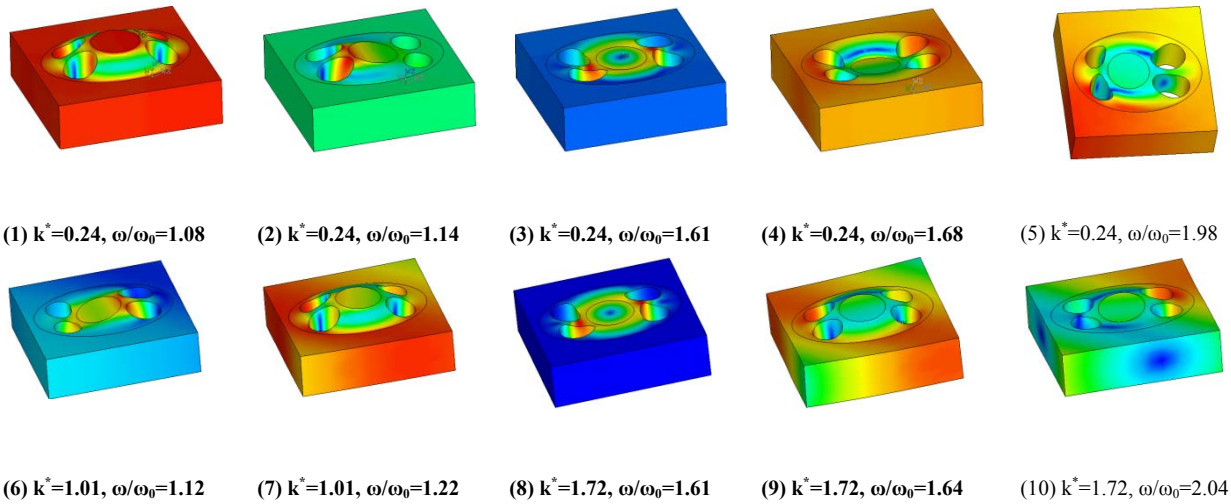

(1) k^*=0.24, ω/ω_0=1.08 (2) k^*=0.24, ω/ω_0=1.14 (3) k^*=0.24, ω/ω_0=1.61 (4) k^*=0.24, ω/ω_0=1.68 (5) k^*=0.24, ω/ω_0=1.98

(6) k^*=1.01, ω/ω_0=1.12 (7) k^*=1.01, ω/ω_0=1.22 (8) k^*=1.72, ω/ω_0=1.61 (9) k^*=1.72, ω/ω_0=1.64 (10) k^*=1.72, ω/ω_0=2.04

(b)

FIG. 14. (a) Comparison of the dispersion curves obtained by the continuum model and the FE simulation for the guided wave propagation along 45 degree with respective to the principal direction; (b) The displacement fields around several gap-edge modes in the points 1-10.

Based on the developed continuum model, we will further study the wave behavior of the anisotropic EMM plate such as existence of preferential directions of effective velocities and energy flow. Figs. 15 (a) and (b) show the slowness curves of both symmetric and anti-symmetric waves in the metamaterial plate at three different frequencies, respectively. In the figures, ω_0 is the locally resonant angular frequency of the microstructure along x_1 direction, $c_T^0 = \sqrt{C_{66}/\rho^0}$ is the in-plane bulk transverse wave velocity and ρ^0 is the static mass density of the plate. In the example, the microstructure design proposed in Fig. 3 (a) is chosen with lead, rubber and epoxy as the core, coating and matrix materials, respectively. From the Fig. 15 (a), we notice that the anisotropy of effective velocities is obvious; the effective velocity along x_1 direction is higher than that along x_2 direction. For the frequencies at $\omega/\omega_0 = 0.14$ and 0.7, the shapes of the slowness curves indicate strong energy focusing along specific $x_1$and x_2 directions. For the frequency at $\omega/\omega_0 = 2.0$, the anisotropy increases and most energy will propagate along x_1 direction. However, for antisymmetric wave, as shown in Fig. 15 (b), changes in the shapes of slowness curves can be found at the three different frequencies.

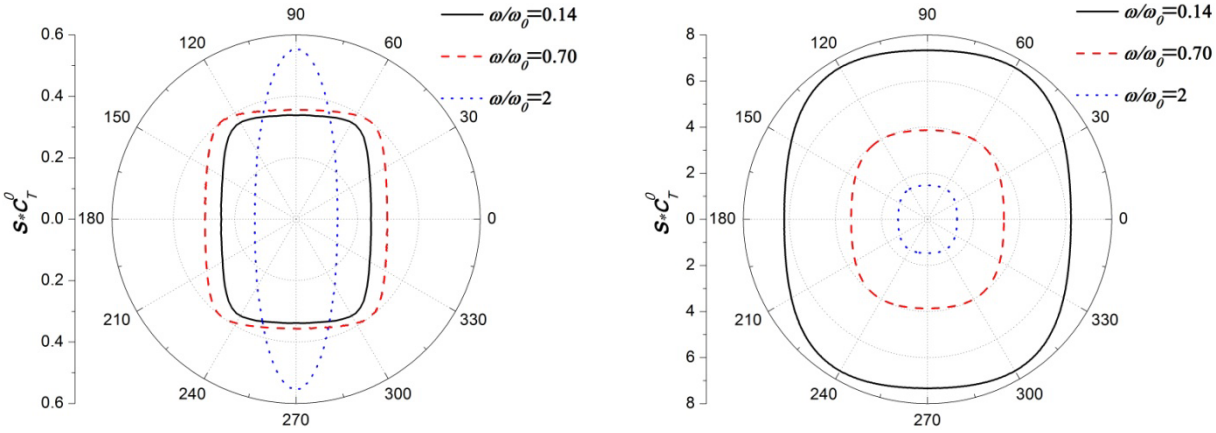

(a) Symmetric wave (b) Antisymmetric wave

FIG. 15. Slowness curves of symmetric and antisymmetric wave at different frequencies

In order to further evaluate the difference between the phase direction and energy direction quantitatively at different frequencies, the energy flow direction as a function of phase direction angle is plotted in Fig. 16. For simplicity but without loss of generality, we assume that the guided wave is propagating along x-axis which has an angle δ with respect to the principal x_1-axis and $\theta = tan^{-1}(\frac{\partial\omega/\partial k_y}{\partial\omega/\partial k_x})$ is the difference between the group velocity direction and the phase velocity direction. It can be noticed that the relation between the directions of phase velocity and group velocity is almost invariable for the antisymmetric wave at different frequencies, which explains the consistence of the shapes of slowness curves in Fig. 15 (b). In contrast with the results of the antisymmetric wave, the relations between the directions of phase velocity and group velocity for different symmetric wave modes change obviously at different frequencies in Fig. 16, which is also consistent with the result shown in Fig. 15 (a). It should also be noticed that except for the two principal directions, the zero value of θ, which represents that the energy propagation direction is parallel to the phase direction, also occurs when the first symmetric wave (black circle and red triangle) propagates along the direction that deviates at 50° to 60° from the principal x_1-axis. However, no energy flow propagates parallel to the phase direction when the propagation direction of the second symmetric wave mode (blue square) does not coincide with either principal direction of the EMM plate.

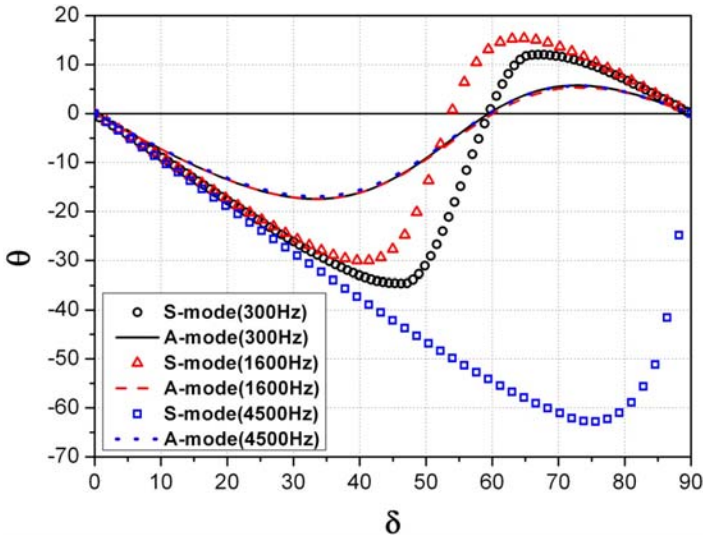

FIG. 16. Energy direction θ with respect to the phase direction δ for symmetric and antisymmetric wave propagations at various frequencies

V. CONCLUSION

This paper presented a new microstructure design and conducted an experimental validation of wave propagation in an EMM plate with anisotropic effective mass density. The design was achieved via numerically-based effective medium model. The experimental validation was conducted in the EMM plate through the analysis of the harmonic and transient wave propagation. The group and phase velocities as functions of frequency were obtained from transmission measurements of the transient wave signals with the aid of the wavelet technology, from which the effective mass densities along the two principal directions of the proposed EMM plate were then experimentally demonstrated for the first time. Excellent agreements between the experimental results and those from the numerically-based effective medium model were observed. Finally, a continuum model of guided wave propagation in the anisotropic EMM plate has been developed. The continuum model can correctly predict different guided wave modes in the EMM plate, which are difficult to be measured experimentally. Particularly, the high-order guided wave coupling and repulsion as well as the preferential energy flow direction in the anisotropic EMM plate were discussed.

Acknowledgment

This work was supported in part by Air Force Office of Scientific Research under Grant No. AF 9550-10-0061 with Program Manager Dr. Byung-Lip (Les) Lee and NSF EAGER program No. 1037569.

REFERENCE

[1] Z. Liu, X. Zhang, Y. Mao, Y. Y. Zhu, Z. Yang, C. T. Chan, and P. Sheng, Science, **289**, 1734 (2000).

[2] X. Hu, C. T. Chan, and J. Zi, Phys. Rev. E **71**, 055601 (2005).

[3] N. Fang, D. Xi, J. Xu, M. Ambati, W. Srituravanich, C. Sun, and X. Zhang, Nature Mater. **5**, 452 (2006).

[4] P. F. Pai, J. Intell. Mater. Syst. Struct. **21**, 517 (2010).

[5] D. Torrent and J. Sa´nchez-Dehesa, New J. Phys. **9**, 323 (2007).

[6] S. Zhang, L. L. Yin, and N. Fang, Phys. Rev. Lett. **102**, 194301 (2009).

[7] S. Gonella, A. C. To, and W. K. Liu, J. Mech. Phys. Solids **57**, 621 (2009).

[8] A. P. Liu, R. Zhu, X. N. Liu, G. K. Hu, and G. L. Huang, Wave Motion **46**, 411 (2012).

[9] S. A. Cummer and D. Schurig, New J. Phys. **9**, 45 (2007).

[10] M. Schoenberg and P. N. Sen, J. Acoust. Soc. Am. **73**, 61(1983).

[11] Y. Cheng, F. Yang, J. Y. Xu, and X. J. Liu, Appl. Phys. Lett. **92**, 151913 (2008).

[12] D. Torrent and J. Sánchez-Dehesa, Phys. Rev. Lett. **103**, 064301(2009).

[13] D. Torrent and J. Sa′nchez-Dehesa, New J. Phys. **10**, 023004 (2008).

[14] J. B. Pendry and J. Li, New J. Phys. **10**, 115032 (2008).

[15] L. Zigoneanu, B. I. Popa, and S. A. Cummer, J. Appl. Phys. **109**, 054906 (2011).

[16] Z. Liu, C. T. Chan, and P. Sheng, Phys. Rev. B **71**, 014103 (2005).

[17] G. W. Milton and J. R. Willis, Proc. R. Soc. A **463**, 855 (2007).

[18] G. W. Milton, New J. Phys. **9**, 359 (2007).

[19] P. Sheng, X. X. Zhang, Z. Y. Liu, and C. T. Chan, Physica B **338**, 201 (2003).

[20] Y. Gu, X. Luo, and H. Ma, J. Appl. Phys. **105**, 044903 (2009).

[21] H. H. Huang and C. T. Sun, Philos. Mag. **91**, 981 (2011).

[22]Y. Wu, Y. Lai, and Z. Q. Zhang, Phys. Rev. Lett. **107**, 105506 (2011).

[23] Y. Lai, Y. Wu, P. Sheng, and Z. Q. Zhang, Nature Mater. **10**, 620 (2011).

[24] X. M. Zhou and G. K. Hu, Phys. Rev. B **79**, 195109 (2009).

[25] X. N. Liu, G. K. Hu, and C. T. Sun, J. Vib. Acoust. **330**, 2536 (2011).

[26] M. Hirsekorn and P. P. Delsanto, J. Appl. Phys. **99**, 124912 (2006).

[27] S. Nemat-Nasser, J. R. Willis, and A. V. Amirkhizi, Phys. Rev. B **83**, 104103 (2011).

[28] F. Song, G. L. Huang, and K. Hudson, Smart Mater. Struct. **18**, 125007 (2009).

[29] M. Sato, J. Acoust. Soc. Jpn. **47**, 405 (1991).